

## Research Paper

## Research on the Acoustic Scattering Characteristics of Multi-Sections Conning Tower Geometries in Monostatic Configuration

Lin-Jiang HAN<sup>(1)</sup>, Hao SONG<sup>(2)</sup>, Chang-Xiong CHEN<sup>(1)</sup>, Xi-Rui PENG<sup>(3)</sup>, Zi-Long PENG<sup>(1)\*</sup><sup>(1)</sup> *Jiangsu University of Science and Technology*  
Zhenjiang 212100, China<sup>(2)</sup> *Systems Engineering Research Institute*  
Beijing 100036, China<sup>(3)</sup> *China Ship Development and Design Center*  
Wuhan 430064, China

\*Corresponding Author e-mail: zlp\_just@sina.com

(received January 18, 2022; accepted April 26, 2022)

The overall acoustic echo of a submarine is greatly dependent on the conning tower. For enhancing the acoustic stealth performance of a submarine, it is necessary to research an innovative design scheme of the conning tower to reduce its target strength (TS). The aim of this work is to reduce the TS of a conning tower by varying its geometry and streamlining. The accuracy in modelling the acoustic scattering of a conning tower using the Kirchhoff approximation (KA) was validated, compared with finite element analysis (FEA). Several angular conning tower geometries were designed to analyze the effect of streamlining and the number of lateral facets on TS using the KA method. In consideration of the actual situation, the acoustic effect of backing medium was analyzed by compared water-filled elastic hulls with rigid hulls. From the observed TS calculation results, it is shown that the non-streamlined four lateral-facet conning tower geometries are optimal for acoustic stealth performance during the range of incidence angles from  $-10^\circ$  to  $10^\circ$ , whereas the streamlined versions have better performance at incidence angles beyond this range. Furthermore, elastic hulls and rigid hulls provide similar spatial distribution regularities in monostatic configuration with the rigidity affecting the magnitude of the TS.

**Keywords:** conning tower; Kirchhoff approximation; target strength; monostatic configuration.



Copyright © 2022 L.-J. Han *et al.*  
This is an open-access article distributed under the terms of the Creative Commons Attribution-ShareAlike 4.0 International (CC BY-SA 4.0) <https://creativecommons.org/licenses/by-sa/4.0/> which permits use, distribution, and reproduction in any medium, provided that the article is properly cited, the use is non-commercial, and no modifications or adaptations are made.

## 1. Introduction

As one of the largest protruding components, the conning tower generally makes a significant contribution to the overall acoustic echo of submarine (SUN *et al.*, 2012; PAN, DENG, 2020; HU, ZENG, 2015; HU, 2017). The reduction of TS is a crucial mission for a submarine to avoid being detected by active sonar. According to the active sonar equation, the TS reduction of a submarine will significantly decrease the range detected from the enemy (ZHONG, XU, 2006; HE, 2006; ZHU, GUO, 2014; YAN *et al.*, 2020). Some technologies are utilized to achieve this aim including shaping stealth (LI *et al.*, 2020), anechoic coatings (FENG *et al.*,

2019), and acoustic metamaterials (ZHANG *et al.*, 2009; LI *et al.*, 2015; Wang, 2020). However, few studies focus on the shaping stealth with respect to the conning tower by altering its streamlining and geometry, while satisfying all performance and deployment requirements.

Various numerical methods can be used to deal with acoustic scattering problems. For example, FEA and boundary element method (BEM) are both able to compute highly accurate acoustic scattering results at low and medium frequencies (SCHNEIDER *et al.*, 2003; CAO *et al.*, 2015; YANG, WANG, 2007; ZHAO, REN, 2020; XU *et al.*, 2015; FENG *et al.*, 2018; CHEN, LUO, 2018). It is at the expense of extremely

dense grids to ensure sufficient accuracy, and this required grid density increases with analysis frequency (MARBURG, 2002; ZHOU, WEN, 2020; ZHOU *et al.*, 2020; LI, LI, 2020). Since the conning tower is relatively large-sized, a tremendous computation would be required with FEA or BEM. However, for high-frequency acoustic scattering problems, the KA method is an ideal choice considering the computational efficiency demonstrated to be highly accurate (FAN *et al.*, 2012). The KA method was subsequently improved considering secondary scattering and occlusion (ZHENG *et al.*, 2011), and used to predict TS of underwater complex targets with relatively high accurate (FENG, 2010, SUN *et al.*, 2016). An echo highlight simulation method was proposed based on the KA method (LIU, 2012).

In this study, the contribution of the conning tower to the overall acoustic echo of submarine is described and some numerical methods dealing with acoustic scattering are compared at first. In Sec. 2, the TS calculation formulas are derived with the KA for rigid and elastic targets. In Sec. 3, the calculations of the underwater acoustic scattering field based on KA method are verified with experiments and FEM. In Sec. 4, models for predicting the TS of conning towers were constructed based on various multi-sections conning tower geometries. The geometry of the conning tower was varied in terms of number of facets, facet angle and streamlining. The relationship between the geometry and TS of the conning tower is analyzed with KA method. Some suggestions for minimizing the TS of a conning tower are then provided based on these results, and the optimal streamlining type for each sonar detection configuration is researched. Finally, a summary and a discussion of the results are presented in Sec. 5.

## 2. Materials and methods

The KA method is based on two fundamental assumptions (TANG *et al.*, 2018). For assumption 1, the scattering surface can be categorized into illuminated and shadow regions. The illuminated region scatters acoustic waves, while the shadow region does not. For assumption 2, the illuminated region can be meshed into localized planar elements. The overall echo from a region depends on the reflection characteristics of these constituent planar elements.

As shown in Fig. 1, the sound wave is incident on the surface  $S$  from  $M_1$ . Since the time-varying acoustic pressure can be decomposed into the superposition of various spectral components represented by time dependence, with time dependence of all quantities assumed as  $e^{i\omega t}$ , where  $\omega$  is the angular frequency and  $t$  is time, the time dependence can be omitted in the discussion. Therefore, the incident wave potential function is  $\phi_i = Ae^{ikr_1}/r_1$ , where  $A$  is an amplitude, and the scattered sound field of  $M_2$  is  $\phi_s$ . The distances from

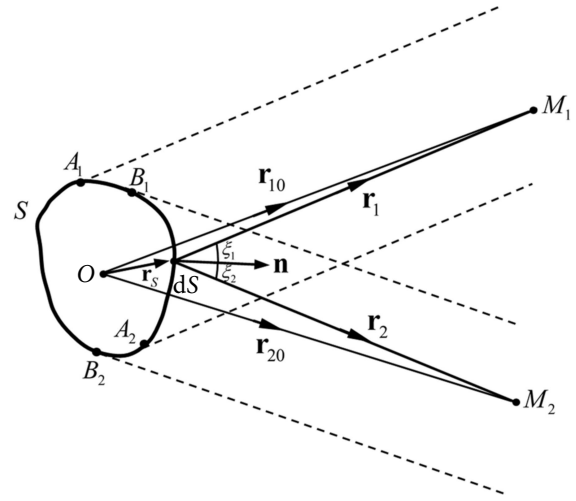


Fig. 1. Schematic diagram of acoustic scattering for deriving KA.

the surface element  $dS$  to  $M_1$  and  $M_2$  are  $r_1$  and  $r_2$ , respectively. The illuminated regions from  $M_1$  and  $M_2$  are  $A_1$ – $A_2$  and  $B_1$ – $B_2$ , respectively, and the common illuminated region is  $B_1$ – $A_2$ . The distances from the origin of coordinates  $O$  to  $M_1$  and  $M_2$  are denoted by  $r_{10}$  and  $r_{20}$ , respectively.  $\mathbf{n}$  is the external normal of the surface  $S$ .  $\xi_1$  and  $\xi_2$  are the angles between  $r_1$ ,  $r_2$  and  $\mathbf{n}$ , respectively.

In monostatic configuration,  $|\mathbf{r}_1| = |\mathbf{r}_2| = r$ ,  $|\mathbf{r}_{10}| = |\mathbf{r}_{20}| = r_0$ , and  $\xi_1 = \xi_2 = \xi$ . According to KA method, the integral surface  $S$  should be defined as illuminated regions, the acoustic scattering field satisfies:

$$\phi_s(r) = \frac{ikA}{2\pi} \int_S \frac{e^{ik2r}}{r^2} \cos \xi \, dS, \quad (1)$$

where  $\xi$  varies from the surface points. In the far field,  $r$  can be approximated as  $r = r_0 + \Delta r$  in the exponent and  $r \approx r_0$  in the denominator, which yields:

$$\phi_s(r) = -\frac{ikA}{2\pi} \frac{e^{ik2r_0}}{r_0^2} \int_S e^{ik2\Delta r} \cos \xi \, dS. \quad (2)$$

In the far field, their path difference can be approximated as  $\Delta r = r - r_0 \approx \frac{\mathbf{r}_s \cdot \mathbf{r}_0}{r_0}$ , where  $\mathbf{r}_s$  is the radius vector of surface element  $dS$ , and  $\frac{\mathbf{r}_0}{r_0}$  is the unit vector from  $O$  to  $M_1$ . Let  $I$  represent the integral:

$$I = \int_S e^{ik2\Delta r} \cos \xi \, dS = \int_S e^{2ik \frac{\mathbf{r}_s \cdot \mathbf{r}_0}{r_0}} \left( \mathbf{n} \cdot \frac{\mathbf{r}_0}{r_0} \right) dS. \quad (3)$$

Considering the rigid surface, the backscattering cross section can be defined:

$$\sigma_s = \lim_{r_0 \rightarrow \infty} \left( 4\pi r_0^2 \left| \frac{\phi_s}{\phi_i} \right|^2 \right) = \frac{k^2}{\pi} |I|^2, \quad (4)$$

where  $k = \frac{2\pi}{\lambda}$ , and  $\lambda$  is acoustic wavelength. Thus, the TS can be expressed as:

$$\text{TS} = 10 \log \frac{\sigma_s}{4\pi} = 10 \log \left( \frac{1}{\lambda^2} |I|^2 \right). \quad (5)$$

Considering the non-rigid surface, the scattering wave potential function is

$$\phi_s = -\frac{A}{2\pi} \int_S e^{i2kr} V(\theta) \left( \frac{ikr-1}{r^3} \cos \xi \right) dS, \quad (6)$$

where  $V(\theta)$  is the reflection coefficient.

As shown in Fig. 2, the sound wave is incident on the steel shell with seawater on both sides.  $\theta$  and  $\gamma$  are the angles in terms of dilatational and shear waves respect to the normal. According to Snell's law, the  $x$  component of the wave vector,  $\sigma$  is the same for each layer.  $k$  and  $\kappa$  are P-wave number and S-wave number, respectively. Thus

$$\sigma = k_1 \sin \theta_1 = k_2 \sin \theta_2 = \kappa_2 \sin \gamma_2. \quad (7)$$

The reflection coefficient  $V(\theta)$  can be expressed as (JACKINS, 1986):

$$V(\theta) = \frac{(N^2 - M^2 - 1)^2}{4M^2 + (N^2 - M^2 - 1)^2}, \quad (8)$$

$$M = \frac{Z_2}{Z_1} \cos^2 2\gamma_2 \cot(k_2 d \cos \theta_2) + \frac{Z_{2t}}{Z_1} \sin^2 2\gamma_2 \cot(\kappa_2 d \cos \gamma_2), \quad (9)$$

$$N = \frac{Z_2}{Z_1} \frac{\cos^2 2\gamma_2}{\sin(k_2 d \cos \theta_2)} + \frac{Z_{2t}}{Z_1} \frac{\sin^2 2\gamma_2}{\sin(\kappa_2 d \cos \gamma_2)}, \quad (10)$$

where  $M$  and  $N$  have no physical meaning, just a coefficient,  $\rho_1$  and  $\rho_2$  are the densities of seawater and steel plate, respectively.  $c$  and  $b$  are P-wave velocity and shear-wave velocity, respectively.  $d$  is the thickness of steel plate.  $Z_1$  represents the P-wave impedance of seawater.  $Z_2$  and  $Z_{2t}$  represent P-wave impedance and S-wave impedance of steel, respectively. Their formulas are given as follows:

$$Z_1 = \frac{\rho_1 c_1}{\cos \theta_1}, \quad Z_2 = \frac{\rho_2 c_2}{\cos \theta_2}, \quad Z_{2t} = \frac{\rho_2 b_2}{\cos \gamma_2}. \quad (11)$$

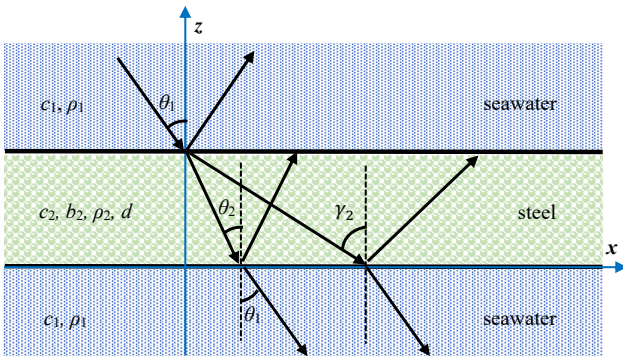


Fig. 2. Schematic diagram of reflection coefficient calculation.

### 3. Comparisons of the KA solutions, FEA solutions and experimental results

#### 3.1. TS comparisons between FEA solutions and KA solutions of conning tower

Two conning tower geometries were used for this comparison, a novel un-smoothed (non-streamlined) multi-sections geometry and a smoothed (streamlined) version of this geometry, as shown in Fig. 3. The results, shown in Figs 4a and 4b, demonstrate that the monostatic TS calculated by the KA method and FEA for the given geometries at normal incidence are very similar at frequencies below 3 kHz. Therefore, it means that the monostatic TS of a multi-sections conning tower can indeed be accurately calculated by the KA method. Furthermore, the results for the smoothed and unsmoothed geometries are similar at frequencies of 100 Hz–2 kHz. However, in the range of 2–3 kHz, the result difference of the two geometries becomes more obvious. Therefore, in order to distinguish the two geometries, it is necessary to consider the higher frequency band above 3 kHz in the subsequent simulation.

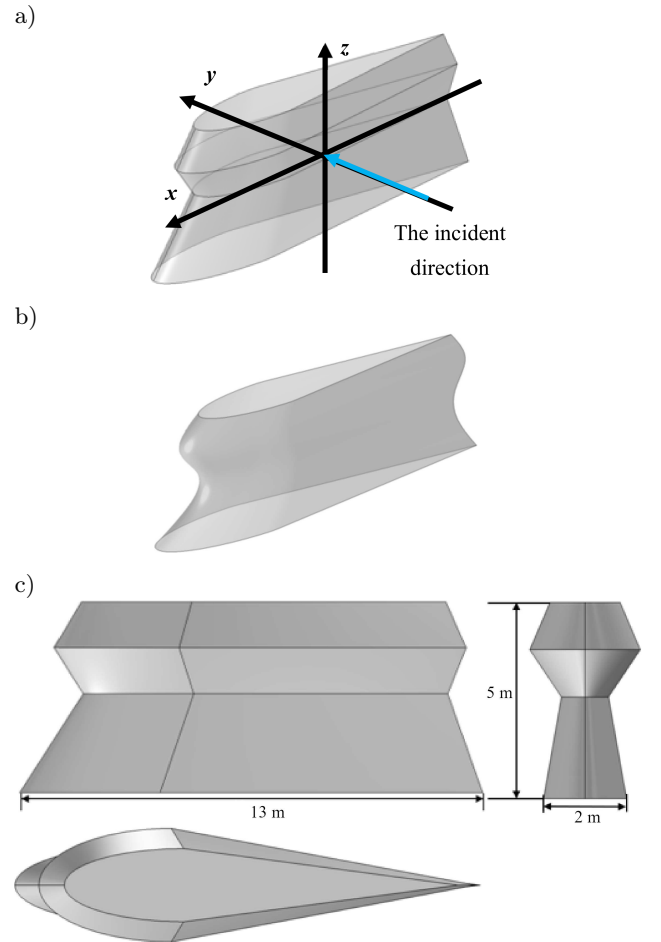


Fig. 3. Two geometries of multi-sections conning tower: a) non-streamlined geometry; b) streamlined geometry; c) three views of unsmoothed geometry.

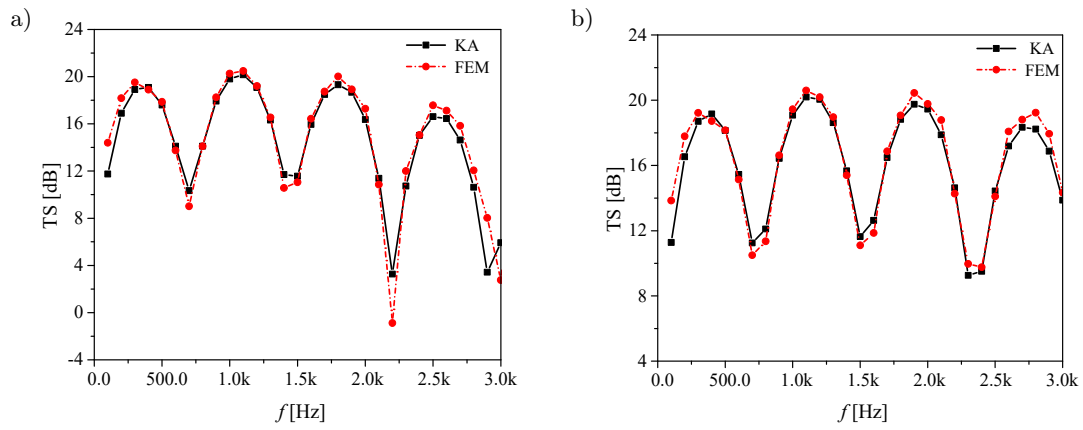


Fig. 4. Monostatic TS of two conning tower at normal incidence: a) non-streamlined conning tower; b) streamlined conning tower.

3.2. TS comparisons between the experimental results and KA solutions of a Benchmark submarine

The specific dimensions of the Benchmark submarine model are shown in Fig. 5, and the test model

is shown in Fig. 6. It is a scale single shell benchmark model with a scaling value of 1:15. The shell material is stainless steel, the thickness of the shell is 3 mm, and its length is 4.13 m. The test equipment is arranged as shown in Fig. 7.

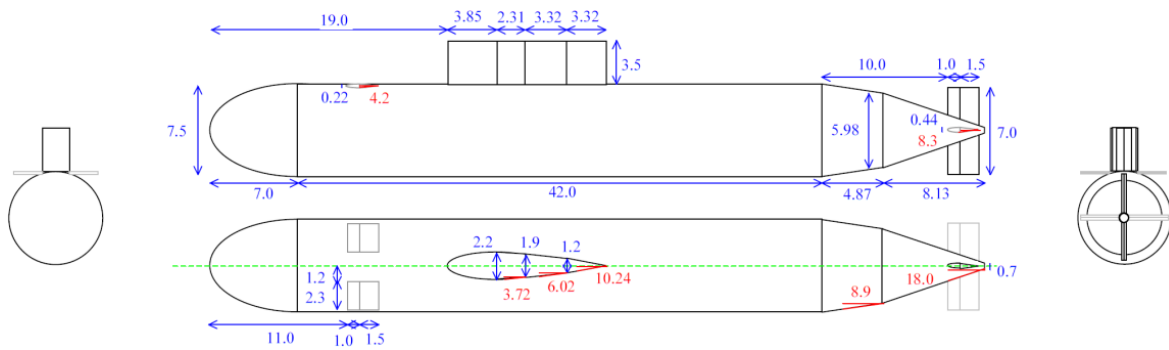


Fig. 5. The specific dimensions of the Benchmark submarine.



Fig. 6. Benchmark submarine mode and testing site.

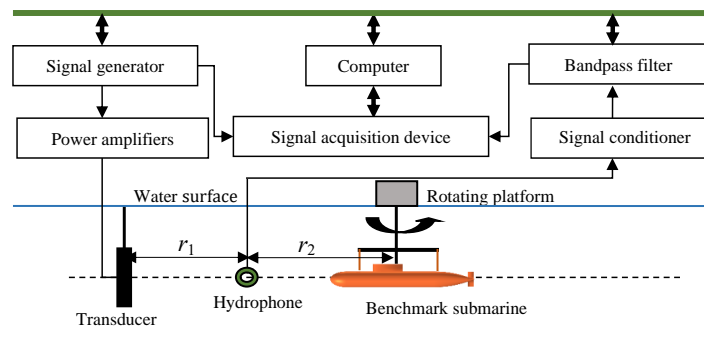


Fig. 7. Test equipment layout.

The TS calculation formula is as follows:

$$\begin{aligned}
 \text{TS} &= 20 \lg \left| \frac{p_{s@1m}}{p_i} \right| = 20 \lg \left| \frac{p_s r_2 (r_1 + r_2)}{p_1 r_1} \right| \\
 &= 20 \lg \left| \frac{V_s r_2 (r_1 + r_2)}{V_1 r_1} \right|, \quad (12)
 \end{aligned}$$

where  $p_s$  and  $p_{s@1m}$  are the echo pressure from Benchmark submarine received by the hydrophone and at 1 m, respectively.  $p_1$  is sound pressure of sound source received by hydrophone.  $r_1$  and  $r_2$  are the distances between hydrophone and transducer or target center,

respectively.  $V_s$  and  $V_1$  are voltage amplitudes of target echo and sound source received by hydrophone, respectively.

The shell is considered as a rigid target in the simulation calculation. TS comparisons of a Benchmark submarine between the experimental results and KA solutions in monostatic configuration are shown in Fig. 8.

As illustrated in Fig. 8, in the range of 3–10 kHz with a step of 1 kHz, the TS directivity of Benchmark submarine presents a butterfly shape for both simulation results and experimental results, that is, the TS is

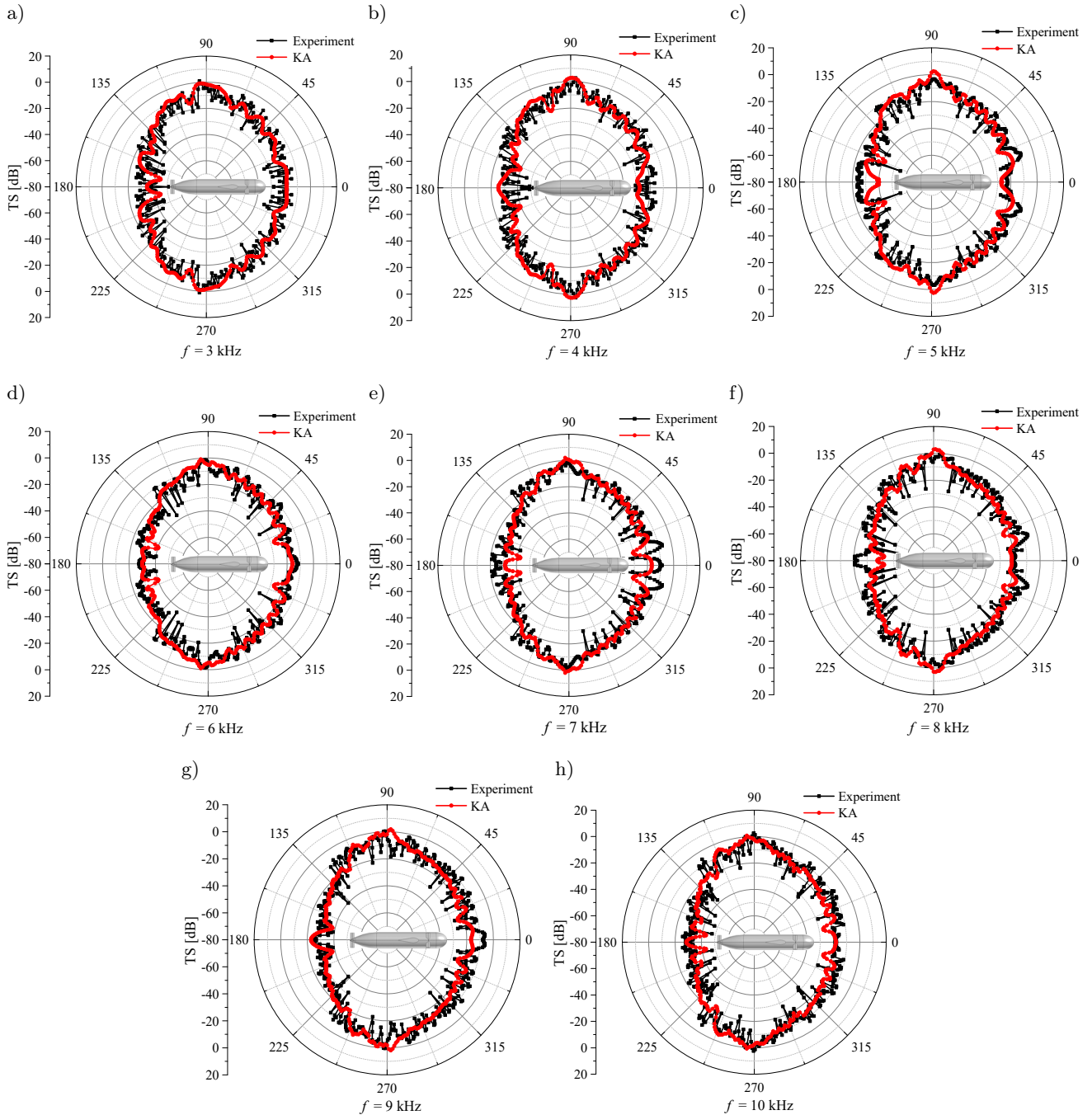


Fig. 8. TS results comparisons between the experimental results and KA solutions.

Table 1. The average TS in different angle ranges [dB].

Frequency [kHz]	0–70°			70–110°			110–180°		
	Experiment	KA	Error	Experiment	KA	Error	Experiment	KA	Error
3	-18.0	-17.4	0.6	-10.4	-7.5	2.9	-25.9	-24.6	1.3
4	-17.6	-19.4	-1.7	-8.1	-7.9	0.3	-25.1	-24.3	0.9
5	-16.6	-18.0	-1.5	-10.6	-7.9	2.6	-24.7	-25.4	-0.8
6	-16.3	-17.4	-1.1	-10.2	-7.4	2.8	-25.1	-25.5	-0.4
7	-16.6	-18.2	-1.6	-8.7	-6.1	2.6	-24.0	-26.6	-2.6
8	-15.2	-17.8	-2.6	-8.5	-6.2	2.4	-24.8	-26.6	-1.8
9	-14.1	-16.8	-2.6	-8.8	-5.9	2.9	-24.3	-24.6	-0.2
10	-15.3	-17.7	-2.4	-7.8	-6.0	1.8	-25.8	-26.2	-0.4

low when the acoustic wave is incident from bow and stern, and highest during the abeam incident. One of the main reasons for this phenomenon is that the conning tower contributes a strong acoustic reflection to the overall echo as its indispensable side size from the abeam view, so the abeam TS of conning tower should be considered in the design of acoustic stealth.

By conducting the acoustic scattering experiment of Benchmark submarine scale model in lake, the experimental results at different frequencies are obtained. From Table 1, the TS average errors between KA solutions and experimental results are within  $\pm 3$  dB with a good agreement.

#### 4. Computational results of the conning tower models

To elucidate the relationship between the TS and the geometry of a conning tower, TS is computed for non-streamlined and streamlined conning tower geometries with four lateral facets. The detection of submarines is generally long-distance anti-submarine detection, and the maximum detection pitch angle generally does not exceed  $\pm 20^\circ$  (AVSIC, 2019). Therefore, this simulation only calculates the TS of the conning tower within  $\pm 20^\circ$  pitch angle.

A three-view diagram of the non-streamlined geometry with four lateral facets is provided in Figs 9 and 10, which shows the definitions of the facet angle  $\alpha$ , and the incident angle  $\theta$ , the color of geometry is only to distinguish different geometries. In Fig. 11a, it is shown that the sum of  $\alpha$  and  $\theta$  is always close to  $90^\circ$  during the value of  $\theta$  corresponding to the maximum TS of this geometry. Thus, as  $\alpha$  increases to  $90^\circ$ , the value of  $\theta$  corresponding to the strongest echo approaches to  $0^\circ$ . This was caused by the increasingly mirror-like lateral surface of the conning tower with increasing  $\alpha$ . It should be noted that the sign (+/-) of the facet angle  $\alpha$  determines whether the range distribution of the main beam  $\theta$  is greater than or less than  $0^\circ$ . Furthermore, the greater the lateral surface, the more intense the acoustic scattering becomes. The

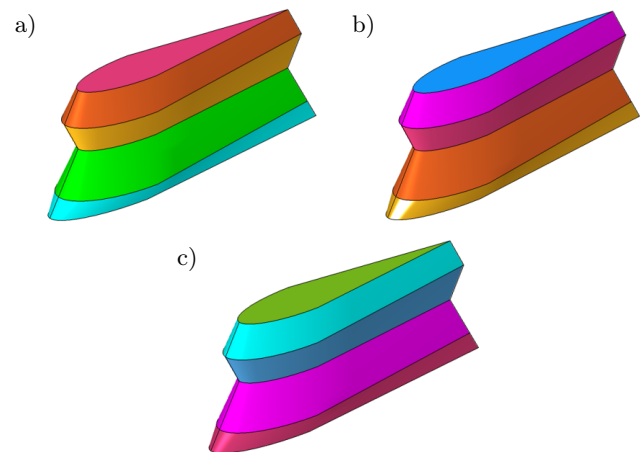


Fig. 9. Non-streamlined four lateral-facet conning tower geometries with different facet angles: a)  $\alpha = 72^\circ$ ; b)  $\alpha = 74^\circ$ ; c)  $\alpha = 76^\circ$ .

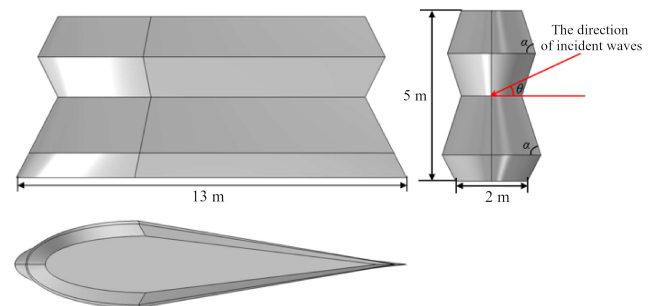


Fig. 10. Three-view diagram of a non-streamlined conning tower geometry with four lateral facets ( $\alpha = 72^\circ$ ).

distribution of acoustic energy peaks with respect to  $\theta$  presents a “feather-like” shape. In Fig. 11b, it is shown that the bandwidth-averaged TS of the non-streamlined four lateral-facet geometry in the range of  $20^\circ$  varies significantly with  $\alpha$ . The main echo beams present around  $\pm 15^\circ$ , or rather at the complementary angle of  $\alpha$ . The TS values of the upper and lower halves are around 16 dB and 11.5 dB due to the asymmetry of both halves. Also, as a reason of the reflection effect from the border lines between lateral facets, there is a strong narrow echo peak from the abeam view with

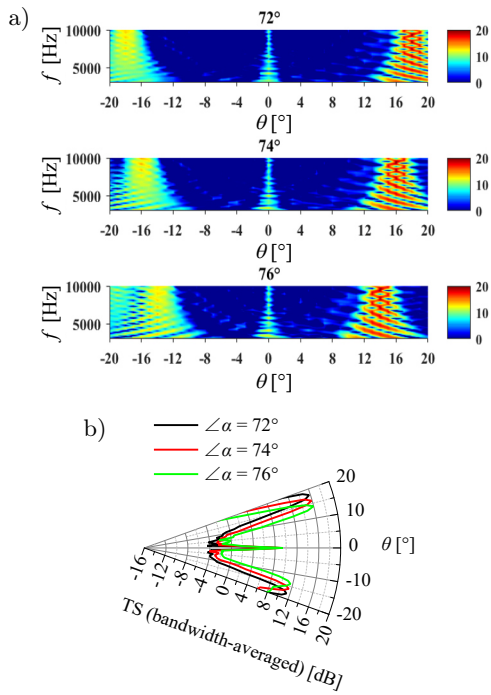


Fig. 11. TS results of non-streamlined four lateral-facet geometries with different  $\alpha$  values: a) angular frequency spectrum of TS; b) echo vertical directivity of TS.

a value around 10 dB. No matter the change of  $\alpha$ , the bandwidth average TS of the three conning towers has a similar change trend with the change of  $\theta$ , and as  $\alpha$  decreases by  $2^\circ$ , the angle of obtaining the maximum moves outwards by  $2^\circ$ . It is also apparent that the geometry with the  $\alpha$  value of  $72^\circ$  has the lowest TS from the three tested models with different  $\alpha$  values in the  $\theta$  range of  $\pm 20^\circ$ .

The streamlined four lateral-facet conning tower geometries with different facet angles are shown in Fig. 12. In monostatic configuration, the acoustic energy distribution of the streamlined geometry accord-

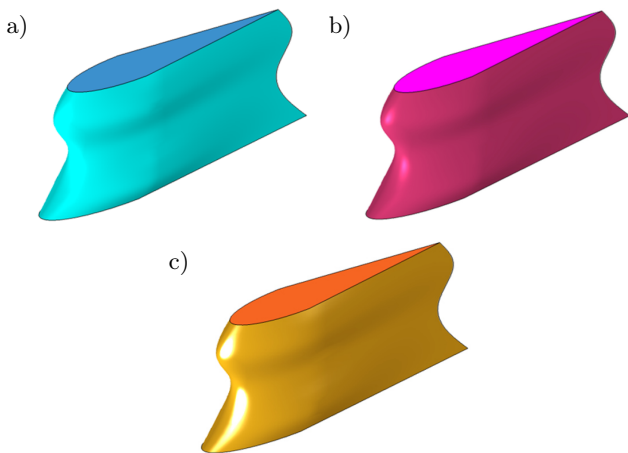


Fig. 12. Streamlined four lateral-facet conning tower geometries with different facet angles: a)  $\alpha = 72^\circ$ ; b)  $\alpha = 74^\circ$ ; c)  $\alpha = 76^\circ$ .

ing to  $\theta$  is largely the same as that of the non-streamlined geometry (Fig. 13a). Their echo energy is not tightly gathered in certain ranges of  $\theta$  compared with the non-streamlined geometry. In Fig. 13b, to be precisely the same to the non-streamlined configuration, the reflection effect from the border lines between lateral facets also makes a strong narrow echo peak from the abeam view with a value around 10 dB. As  $\theta$  gradually varies to both ends, the TS first decreases suddenly, then gradually increases to the maximum, and finally decreases gradually. But the most obvious difference is that the valley zone has been widened compared with the non-streamlined geometry. It can be observed that, the bandwidth average TS pattern of the three conning towers has a similar change trend with the change of  $\theta$ , and the bandwidth-averaged TS of the streamlined conning tower geometry with four lateral facets is the smallest with the  $\alpha$  value of  $72^\circ$  in the  $\theta$  range of  $\pm 20^\circ$ .

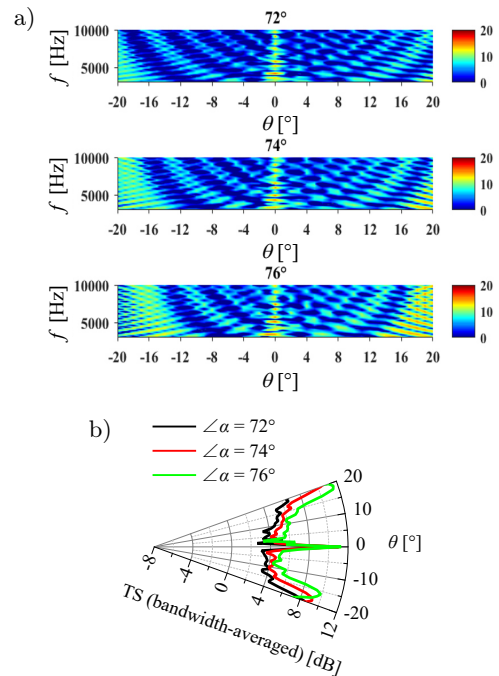


Fig. 13. Comparison of TS of streamlined four lateral-facet geometries with different  $\alpha$  values: a) angular frequency spectrum of TS; b) echo vertical directivity of TS.

A three-view diagram of the non-streamlined conning tower geometry with eight lateral facets and the definitions of  $\alpha$  and  $\theta$  angles are shown in Figs 14 and 15. In Fig. 16 it is shown that the echo distribution of the non-streamlined eight lateral-facet geometry behaves similarly to that of the non-streamlined four lateral-facet geometry, that is, the echo energy concentrations gradually shifted towards to  $0^\circ$  with  $\alpha$ , and the echo distribution shows a “feather-like” pattern with respect to  $\theta$ . Furthermore, the number of “feathers” decreases with  $\alpha$  values. As  $\theta$  gradually varies to both ends, similar to the four lateral-facet-geometry,

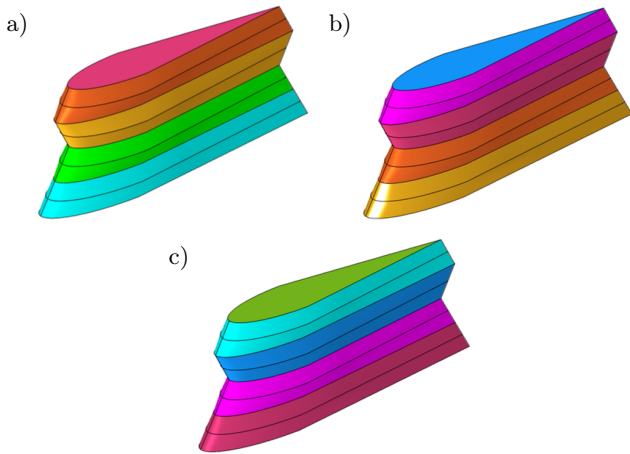


Fig. 14. Non-streamlined eight lateral-facet conning tower geometries with different facet angles: a)  $\alpha = 72^\circ$ ; b)  $\alpha = 74^\circ$ ; c)  $\alpha = 76^\circ$ .

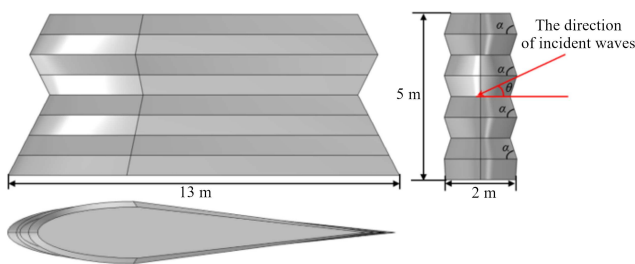


Fig. 15. Three-view diagram of a non-streamlined conning tower geometry with eight lateral facets ( $\alpha = 72^\circ$ ).

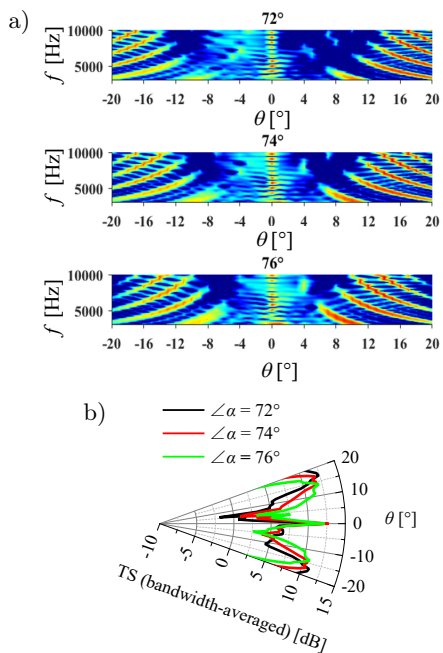


Fig. 16. Comparison of TS of non-streamlined eight lateral-facet geometries with different  $\alpha$  values: a) angular frequency spectrum of TS; b) echo vertical directivity of TS.

the TS first decreases suddenly near  $\pm 5^\circ$ , then gradually increases to a larger value near  $\pm 15^\circ$ , and finally decreases gradually.

The streamlined eight lateral-facet conning tower geometries with different facet angles are shown in Fig. 17. In Fig. 18 it is shown that the TS of the streamlined eight lateral-facet geometries is like their non-streamlined counterparts. The distribution of TS in the former is slightly more homogenous than that in the latter. The effect of  $\alpha$  on the streamlined eight lateral-facet geometry is shown in Fig. 18b to be identical to those on the non-streamlined geometry, that is, the overall bandwidth-averaged TS generally decreased with  $\alpha$ . The variation trend of TS with  $\theta$  is similar to non-streamlined geometry, but the differences between peaks and valleys become smaller for the streamlined geometries.

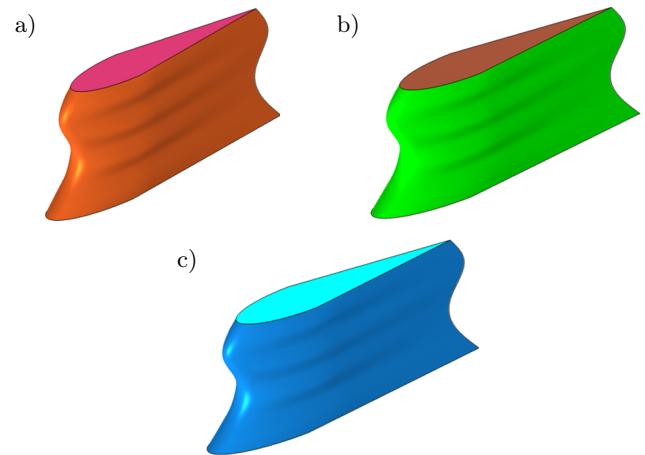


Fig. 17. Streamlined eight lateral-facet conning tower geometries with different facet angles: a)  $\alpha = 72^\circ$ ; b)  $\alpha = 74^\circ$ ; c)  $\alpha = 76^\circ$ .

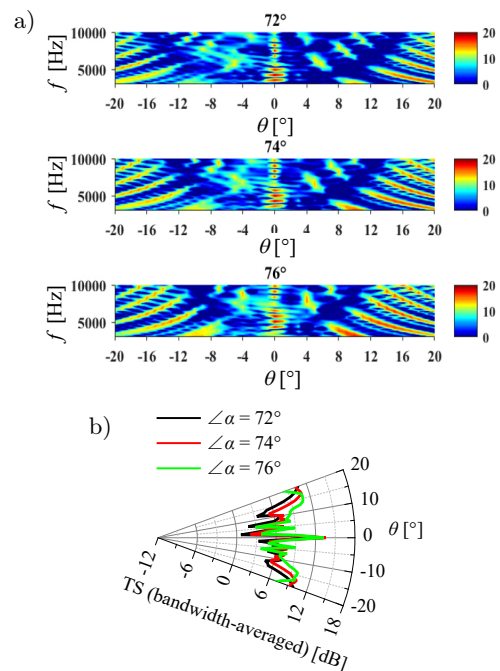


Fig. 18. Comparison of TS of streamlined eight lateral-facet geometries with different  $\alpha$  values: a) angular frequency spectrum of TS; b) echo vertical directivity of TS.

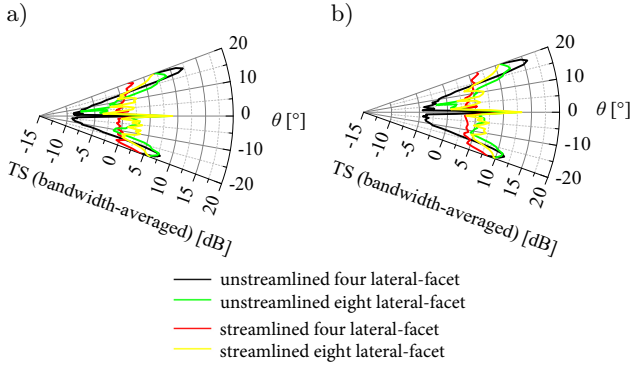


Fig. 19. Echo vertical directivity of TS bandwidth-averaged at 3–10 kHz: a) elastic hull configuration; b) rigid hull configuration.

The TS comparisons of all four multi-sections conning tower geometries are shown for elastic (a water-filled non-pressure-resistant structure) and rigid hulls in Figs 19, 20, and Table 2, in which all evaluated geometries exhibited excellent acoustic stealth properties in the range of  $\pm 10^\circ$  for  $\theta$ , regardless of hull types.

A minor 4 dB reduction in TS was observed for an elastic hull compared with the rigid configuration, as a reason of the elastic conning tower geometries is filled with water. This phenomenon can be roughly explained as follows, the transmission coefficient of acoustic wave increases and the reflection coefficient decreases, considering that the acoustic wave is vertically incident on the infinite plate, the average reflection coefficient is 0.6 in the frequency band of 3–10 kHz, according to Eqs (7)–(11). The TS of the infinite rigid plate is 4.3 dB lower than that of the elastic plate, which is close to the simulation results of the conning tower geometries.

After comparison, it is easy to find that in the range of  $\pm 10^\circ$  for  $\theta$ , whether it is elastic or rigid, the non-streamlined four lateral-facet conning tower geometries have the best acoustic stealth properties, because they can distribute the strong echo regions beyond  $\pm 10^\circ$ , and the TS is lowest at the  $\theta$  value of  $0^\circ$ . But if the detection sonar is located at some position beyond the range of  $\pm 10^\circ$  for  $\theta$ , the streamlined version of these conning tower can be considered optimal for acoustic stealth.

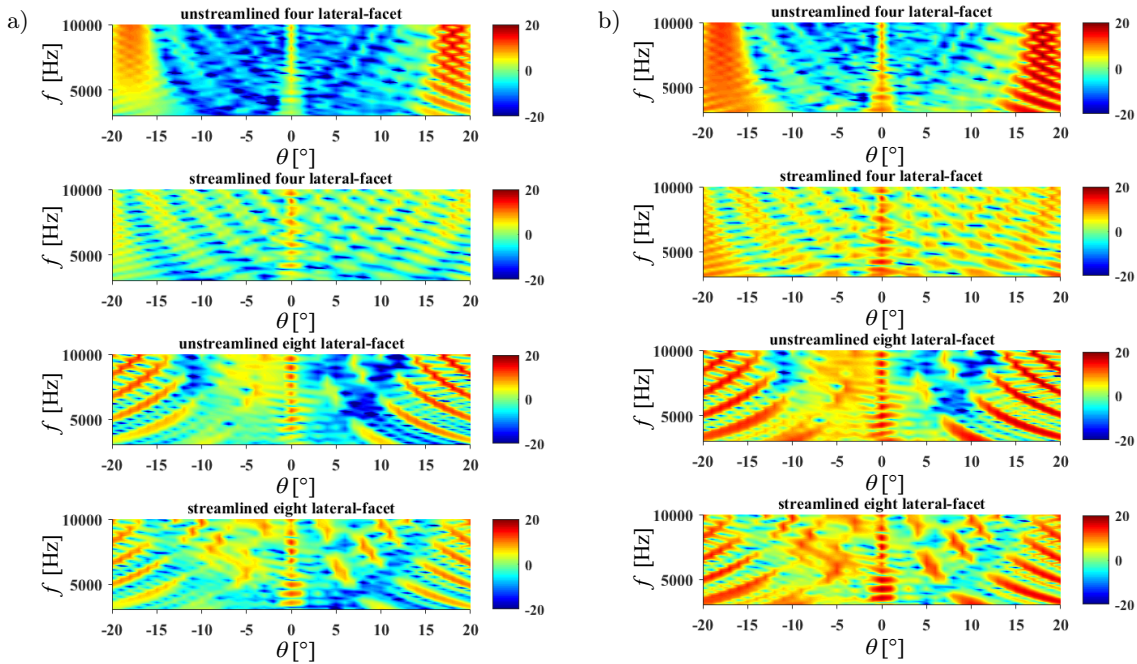


Fig. 20. Angular frequency spectrum of streamlined/non-streamlined conning tower geometries with four/eight lateral facets ( $\alpha = 72^\circ$ ): a) elastic hull configuration; b) rigid hull configuration.

Table 2. TS comparison of elastic and rigid streamlined/non-streamlined conning tower geometries with four/eight lateral facets ( $\alpha = 72^\circ$ ) with an incident angle of  $0^\circ$ .

Case	Four lateral-facet		Eight lateral-facet	
	Non-streamlined [dB]	Streamlined [dB]	Non-streamlined [dB]	Streamlined [dB]
Elastic	4.8	7.1	8.3	9.0
Rigid	8.8	11.0	12.3	13.2
Difference	4.0	3.9	4.0	4.2

## 5. Conclusions

In this study, the echo characteristics of a variety of conning tower geometries were evaluated to determine the full frequency range of geometric effect with the KA method. The findings of this study are expected to help improve the simulation efficiency of acoustic scattering models, particularly in applications related to decreasing the TS of submarines by designing new type conning tower geometries.

In the simulation research of each conning tower geometries, we obtain some conclusions as below.

The monostatic TS of multi-sections conning towers are calculated by the FEA and the KA method. Both solutions are very similar to each other. Furthermore, the KA solutions are in good agreement with the experimental results, which indicates that acoustic scattering modelling with the KA method is accurate enough. Hence, the KA is considered suitable to calculate the TS of complex multi-sections conning towers.

The important factors affecting the TS of a conning tower are supposed to be its facet angle ( $\alpha$ ), type of streamlining and facet design. By analyzing the angular frequency spectrum and echo vertical directivity of the monostatic TS of each conning tower geometry, it was found that angled facets and multi-facet design help to scatter acoustic waves to other directions from the abeam view. Since the angle of obtaining the maximum of TS moves outwards as  $\alpha$  decreases, low  $\alpha$  values are found to be conducive for acoustic stealth close to the incident angle of  $0^\circ$ .

Furthermore, the streamlining is supposed to make the acoustic energy more homogeneously distribute in space and avoid strong mirror-like reflections. Among the evaluated multi-sections geometries, the non-streamlined four lateral-facet geometry is found to provide the best acoustic stealth for sonar in the range of  $\pm 10^\circ$  for  $\theta$ , regardless of whether the hull was elastic or rigid. But if the detection sonar is located at some position beyond the range of  $\pm 10^\circ$  for  $\theta$ , streamlined version of these conning tower can be considered optimal for acoustic stealth.

The monostatic TS of elastic and rigid hulls with the same geometry were essentially similar in terms of their scattering distribution patterns. The only difference is that the elastic hull reduces the TS by approximately 4 dB at most frequencies and angles.

## Acknowledgments

This research was supported by the fund for the Natural Science Youth Foundation of Jiangsu Province (No. BK20200995), the National Defense Science and Technology Foundation Strengthening Program Technology Field Fund (No. 2020-JCJQ-JJ-228), the National Defense Science and Technology Foundation Strengthening Program Technology Key Program

(No. 2020-JCJQ-ZD-222). The authors would like to thank Prof. Jun Fan in Shanghai Jiao Tong University for his suggestions and also the anonymous reviewers for their insightful comments and helpful suggestions made.

## References

1. AVSIC T. (2019), An underwater vehicle shape with reduced acoustic backscatter, [in:] *Proceedings of the 23rd International Congress on Acoustics*, pp. 1935–1941, doi: 10.18154/RWTH-CONV-238818.
2. CAO Y., WEN L., XIAO J., LIU Y. (2015), A fast directional BEM for large-scale acoustic problems based on the Burton–Miller formulation, *Engineering Analysis with Boundary Elements*, **50**(1): 47–58, doi: 10.1016/j.enganabound.2014.07.006.
3. CHEN X., LUO W. (2018), Simulation of scattering acoustic field of underwater target in low-frequency based on ANSYS and SYSNOISE, *Journal of Ordnance Equipment Engineering*, **39**(5): 103–107, doi: 10.11809/bqzbgcxb2018.05.022.
4. FAN J., TANG W.L., ZHUO L.K. (2012), Planar elements method for forecasting the echo characteristics from sonar targets [in Chinese], *Journal of Ship Mechanics*, **16**(1–2): 171–180, doi: 10.3969/j.issn.1007-7294.2012.01.020.
5. FENG Q. (2010), Strength prediction of underwater complicated target based on planar element method [in Chinese], *Torpedo Technology*, **18**(4): 258–262, 267, doi: 10.3969/j.issn.1673-1948.2010.04.005.
6. FENG X.L., CHEN N.R., LI X.W., LI J. (2018), Analyzing the target strength of benchmark submarine by boundary element method at low and middle frequencies [in Chinese], *Technical Acoustics*, **37**(5): 418–424, doi: 10.16300/j.cnki.1000-3630.2018.05.003.
7. FENG X.L., GE X.Y., CHENG Y., WEI N.Y. (2019), Low-frequency target strength analysis of benchmark submarine with acoustic coating [in Chinese], *Ship Science and Technology*, **41**(7): 20–24, doi: 10.3404/j.issn.1672-7649.2019.07.004.
8. HE L. (2006), Development of submarine acoustic stealth technology, *Ship Science and Technology*, (S2): 9–17.
9. HU B. (2017), Research on target strength of submarine sails made by sound-reflecting composites [in Chinese], *Master's thesis of China Ship Research and Development Academy*.
10. HU B., ZENG G.W. (2015), Analysis of substructure echo interference characteristics of benchmark submarine, *Chinese Society of Naval Architecture*, pp. 499–505.
11. JACKINS P.D. (1986), Resonance acoustic scattering from stacks of bonded elastic plates, *The Journal of the Acoustical Society of America*, **80**(6): 1762–1776, doi: 10.1121/1.394291.

12. LI B., PENG Z.L., WEN H.B., FAN J., SONG H. (2020), Research on the optimization design of acoustic stealth shape of the underwater vehicle head, *Acoustics Australia*, **48**(3): 37–47, doi: 10.1007/s40857-019-00170-5.
13. LI J.W., LI W. (2020), Numerical simulation and analysis of target strength of underwater buried objects [in Chinese], *Ocean Engineering Equipment and Technology*, **7**(2): 114–119.
14. LI Y.F., LI W., LI J., WEI K.N., YOU X.J. (2015), Simulation study on acoustic target strength of underwater composite rudders [in Chinese], *Ship & Ocean Engineering*, **44**(4): 21–24, doi: 10.3963/j.issn.1671-7953.2015.04.006.
15. LIU C.Y. (2012), Simulation of echo highlight from underwater target based on the planar element method, *Computer and Digital Engineering*, **40**(5): 146–148.
16. MARBURG S. (2002), Six boundary elements per wavelength: is that enough?, *Journal of Computational Acoustics*, **10**(1): 25–51, doi: 10.1142/S0218396X02001401.
17. PAN M., DENG W. (2020), Research on feature of highlights of submarine echo using simulation method based on planar array [in Chinese], *Ship Electronic Engineering*, **40**(08): 94–97, doi: 10.3969/j.issn.1672-9730.2020.08.023.
18. SCHNEIDER H.G. *et al.* (2003), Acoustic scattering by a submarine: Results from a benchmark target strength simulation workshop, [in:] *Tenth International Congress on Sound and Vibration*, pp. 2475–2482.
19. SUN N.W., LI J.C., WAN Y.M., ZHAO G., LV W., FAN R.N. (2016), Simulation of submarine target strength forecast based on improved planar element method [in Chinese], *Torpedo Technology*, **24**(4): 254–259, doi: 10.11993/j.issn.1673-1948.2016.04.003.
20. SUN X., FAN W., FAN J. (2012), Simulation and experimental verification of acoustic image of echo bright spots for single hull submarine targets [in Chinese], *Journal of Naval University of Engineering*, **24**(06): 26–31.
21. TANG W.L., FAN J., MA Z.C. (2018), Acoustic Scattering of Underwater Target [in Chinese], Science Press, Beijing.
22. WANG X.Q. (2020), The analysis of low frequency acoustic scattering characteristic of composite stiffened cylindrical shells [in Chinese], *Composites Science and Engineering*, (03): 66–69, doi: 10.3969/j.issn.1003-0999.2020.03.010.
23. XU Z.C., ZHANG M.M., WANG L. (2015), Numerical simulation of acoustic scattering at low frequency for the BeTSSi submarine [in Chinese], *Computer & Digital Engineering*, **43**(4): 551–553, 575, doi: 10.3969/j.issn.1672-9722.2015.04.003.
24. YAN D.H., ZHENG H., MIAO J.L. YANG X.G. (2020), Research on submarine stealth technology [in Chinese], *Ship Science and Technology*, **42**(21): 128–133, doi: 10.3404/j.issn.1672-7649.2020.11.026.
25. YANG Z.G., WANG T.Q. (2007), Coupling of exterior/interior field with BEM and numerical simulation of acoustic scattering of fluid target [in Chinese], *Journal of Harbin Engineering University*, **28**(2): 161–164, doi: 10.3969/j.issn.1006-7043.2007.02.009.
26. ZHANG Y.L., TAO M., FAN J. (2009), Target strength calculation of underwater complicated targets coated with absorbing materials [in Chinese], *Journal of Shanghai Jiaotong University*, **43**(8): 1322–1326, 1331, doi: 10.3321/j.issn.1006-2467.2009.08.028.
27. ZHAO X.T., REN C.Y. (2020), Acoustic scattering optimization of underwater shell based on Abaqus and Isight [in Chinese], *Computer Aided Engineering*, **29**(3): 1–6, doi: 10.13340/j.cae.2020.03.001.
28. ZHENG G.Y., FAN J., TANG W.L. (2011), A modified planar elements method considering occlusion and secondary scattering, *Acta Acustica*, **36**(4): 377–383.
29. ZHONG Y.X., XU S.H. (2006), Application and development of stealth technology of naval ship outfitting [in Chinese], *Chinese Journal of Ship Research*, **1**(4): 76–80, doi: 10.3969/j.issn.1673-3185.2006.04.018.
30. ZHOU Y., WEN W. (2020), Application of COMSOL finite element software in acoustic simulation of underwater target [in Chinese], *Computer Applications and Software*, **37**(08): 74–78, 84, doi: 10.3969/j.issn.1000-386x.2020.08.014.
31. ZHOU Y., WEN W., HAN J.H., YANG R.J. (2020), Research on acoustic scattering of underwater complicated target based on sound-solid coupling [in Chinese], *Journal of Unmanned Undersea Systems*, **28**(1): 51–56, doi: 10.11993/j.issn.2096-3920.2020.01.008.
32. ZHU W., GUO H. (2014), Research on the methods of warship stealthy technology [in Chinese], *Ship Electronic Engineering*, **34**(12): 22–26.